

Theoretical Prediction of the Creation and Observation of a Ghost Trilobite Chemical Bond

Matthew T. Eiles,¹ Zhengjia Tong,¹ and Chris H. Greene^{1,2}

¹*Department of Physics and Astronomy, Purdue University, West Lafayette, Indiana 47907, USA*

²*Purdue Quantum Center, Purdue University, West Lafayette, Indiana 47907, USA*



(Received 16 May 2018; published 12 September 2018)

The “trilobite”-type of molecule, predicted in 2000 and observed experimentally in 2015, arises when a Rydberg electron exerts a weak attractive force on a neutral ground state atom. Such molecules have bond lengths exceeding 100 nm. The ultralong-range chemical bond between the two atoms is a nonperturbative linear combination of the many degenerate electronic states associated with high principal quantum numbers, and the resulting electron probability distribution closely resembles a fossil trilobite from antiquity. We show how to coherently engineer this same long-range orbital through a sequence of electric and magnetic field pulses even when the ground-state atom is not present and propose several methods to observe the resulting orbital. The existence of such a *ghost* chemical bond in which an electron reaches out from one atom to a nonexistent second atom is a consequence of the high level degeneracy.

DOI: [10.1103/PhysRevLett.121.113203](https://doi.org/10.1103/PhysRevLett.121.113203)

Many stunning experiments in recent years have demonstrated that a novel type of chemical binding occurs between a highly excited Rydberg atom and a neutral ground-state atom [1–3]. The Fermi pseudopotential reveals that this weak bonding derives from the low-energy scattering of the Rydberg electron off the neutral atom, and furthermore describes this interaction with a delta function proportional to the *s*-wave electron-atom scattering length a_s [4,5]. Rydberg molecules have been observed in Cs, Rb, and Sr, all of which have $a_s < 0$ [1,6,7]. The most interesting Rydberg molecules are the highly polar varieties, dubbed “trilobites” and “butterflies” for the unusual appearance of their electronic densities [8,9]. In these molecules degenerate nonpenetrating high angular momentum l states hybridize to maximize either the electron’s probability (trilobite) or probability gradient (butterfly) near the ground-state atom [2,3,10].

The electronic wave function of one of these molecules having a bond length R_b is

$$\Psi(R_b, \vec{r}) = \mathcal{N} \sum_{l=l_0}^{n-1} c_{nl,x}^b \phi_{nl}(\vec{r}), \quad (1)$$

where \mathcal{N} is a normalization constant, l_0 restricts the summation to degenerate states ($l_0 \approx 3$ in alkali atoms), and $\phi_{nl}(\vec{r}) = [u_{nl}(r)/r]Y_{l0}(\theta, \phi)$ are standard hydrogenic Rydberg wave functions. The label x refers to the type of molecule (i.e., trilobite or butterfly). Because of cylindrical symmetry and the functional form of the pseudopotential, $m_l = 0$. The coefficients $c_{nl,x}^b$ are determined by diagonalizing the Fermi pseudopotential in the basis of degenerate hydrogenic states. For example, $c_{nl,\text{trilobite}}^b = \phi_{nl}(\vec{R}_b)$. For a

general target state these coefficients can be compactly expressed as a vector, \vec{c}_T .

The degeneracy needed to form these exotic states is exact for all l in nonrelativistic hydrogen. Since the hydrogen-electron scattering lengths are both positive, the repulsive trilobite potential curves cannot support vibrational bound states. Nevertheless, theoretical evidence suggests that the Rydberg electron-atom interaction still evinces resonant behavior related to the stationary points of the potential curves [11,12]. These are located at R_b satisfying $u_{n0}(R_b) = 0$ [13]. The index b thus labels a series of trilobite states with specific bond lengths and nodal structure; furthermore, at these R_b the wave function is dominated by just a few eigenfunctions of the Schrödinger equation in elliptical coordinates [14]. Like trilobite molecules, butterfly molecules are bound by electron-atom scattering, although they additionally depend on a *p*-wave shape resonance in the electron-atom scattering and the form of the *p*-wave pseudopotential involves gradient operators acting on the wave function [3,8,9].

This Letter shows that it is possible to create these chemical bonding orbitals with the ground-state atom absent, and for this reason we refer to the electronic wave function [Eq. (1)] as a *ghost chemical bond*. By employing a carefully engineered sequence of alternating magnetic and electric fields, we evolve the wave function from an isotropic ns state into precisely the same orbital that would form a chemical bond if a ground-state atom were located at R_b . The time evolution is described via unitary operators in degenerate first-order perturbation theory. A gradient ascent algorithm derived from optimal control theory optimizes the field sequence to ensure excellent overlap with the target state. Two detection mechanisms are

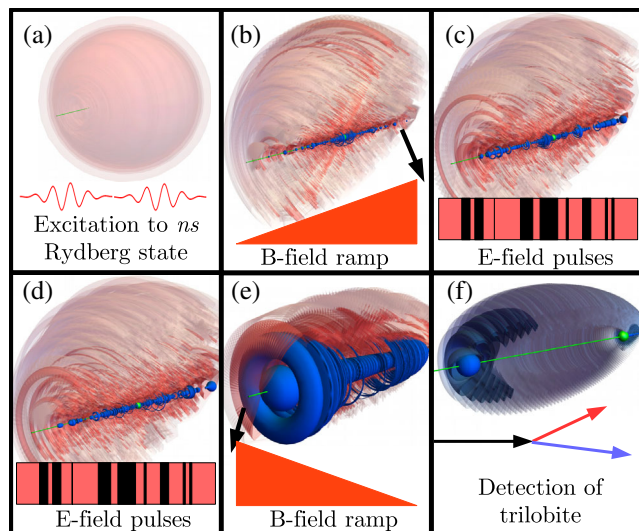


FIG. 1. The proposed scheme, illustrated using the $n = 70$, $b = 1$ trilobite as an example. The electronic probability is displayed in each panel using three isosurfaces, defined where $|\Psi(x, y, z)|^2$ is $C\%$ of $\max(|\Psi_{\text{trilobite}}(R_{b=1}; x, y, z)|^2)$. They are cut away to reveal the inner structure. The Rydberg ion, not to scale, is the green sphere, and the green line, parallel to the z axis, provides a scale and is $1.1 \times 10^4 a_0$ long. The color scheme for panels (a)–(e) is bright blue when $C = 1.54$, red when $C = 0.154$, and translucent pink when $C = 1.54 \times 10^{-2}$. For panel (f), bright blue for $C = 15.4$, darker blue when $C = 1.54$, and transparent blue when $C = 0.308$. (a) First, an ns Rydberg state is created. (b) Next, the magnetic field ramps on, creating a quadratic Zeeman state. (c), (d) After the magnetic field reaches its maximum value, many short electric field pulses are applied in addition to the magnetic field, creating complicated superpositions of the degenerate states. At different points in the sequence the wave function is strongly mixed. (e) At the end of the sequence of electric field pulses, a prototrlobite is created. The magnetic field ramps off and this state evolves into the trilobite state (f), which is detected.

proposed to image and study this chemical bond, either in the “ghost” or in the true trilobite molecule. Atomic units are used throughout.

Figure 1 depicts the proposed experimental implementation of this concept. First, a hydrogen atom is excited to an ns Rydberg state. Next, a magnetic field ramps on to a final amplitude B . Immediately after the ramp, a sequence of N electric field pulses of amplitude F are applied. After the N th pulse the magnetic field ramps off. For the $n = 70$ Rydberg state considered here, the ramp times are typically tens of μs , while the electric field durations and separations are several nanoseconds each, lasting in total several tens of μs as well. This whole process thus occurs within the natural radiative and blackbody lifetime of the Rydberg state. The trilobite state is particularly long-lived since it is an admixture of predominantly high- l states and its decay rate is therefore mostly affected by blackbody radiation. We set a conservative lower lifetime bound at $200 \mu\text{s}$. This time increases with decreasing ambient temperature, extending

to several milliseconds at 10 K [15–19]. As lower l states bleed away, the dominant components of the trilobite state persist, leading to the remarkable scenario where the Rydberg electron remains localized in a small point several hundreds of nanometers away from the proton for many tens of microseconds. Dephasing caused by the small, MHz-scale energy splittings between fine structure levels of the low- l states is limited since these components decay sooner, and additionally this dephasing is further eliminated since the final state is predominately high- l states. These small energy splittings could impact the fidelity as these low- l states are more prominent during the time evolution, but the presence of the large static magnetic field will prevent dephasing between different fine structure states due to the Paschen-Back effect [20]. Interesting effects arise if a small electric field is pulsed on in this final state. The ghost chemical bond will revive every $\tau = (2\pi/3Fn)$, which is about 37 ns for a 0.1 V/cm electric field. Furthermore, the decay mode of the ghost molecule will change as the trilobite state is a linear combination of nondegenerate Stark eigenstates. Details describing the physical considerations guiding this scheme design and some of the relevant parameters are found in the Supplemental Material [20].

Figure 2 displays several ghost chemical bonds which can be created by this scheme. Perhaps the most distinctive characteristic of trilobite bonds is their nodal structure: as b increments by one, a new lobe in the direction perpendicular to the intermolecular axis appears [Fig. 2(a) shows a $b = 3$ trilobite]. Moreover, they are remarkably localized, maximally so in the $b = 1$ trilobite shown in Fig. 1(f), where 20% of the electron density occupies a region around the ghost atom smaller than 0.1% of the total classically allowed volume. This localization is because the trilobite state, by construction, is the representation of the three-dimensional

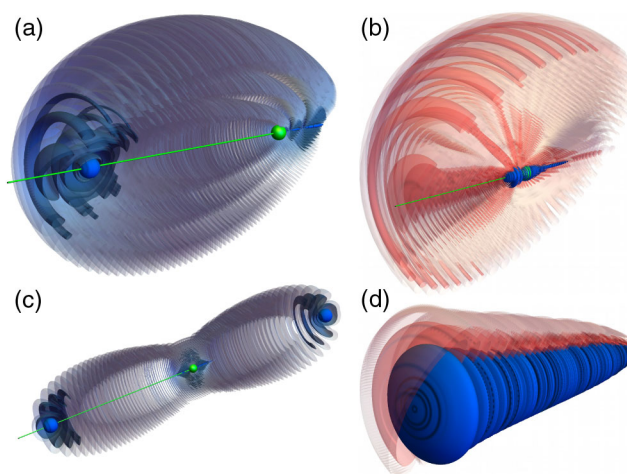


FIG. 2. A gallery of trilobitelike ghost bonds for $n = 70$, shown as isosurfaces as described in the caption of Fig. 1. (a) A $b = 3$ trilobite, (c) an even-parity collinear $b = 1$ trilobite trimer. (b) A butterfly with $R_0 = 653$, (d) the deepest Stark state.

delta function in the finite basis of hydrogenic states in a single n manifold. The butterfly molecule chemical bond [Fig. 2(b)] has a bond length an order of magnitude smaller than the trilobite, and the wave function, fanning out into a winglike structure, fills much more of the classically allowed volume. Rydberg molecules need not be exclusively diatomic: polyatomic Rydberg trilobite or butterfly molecules with more than one ground-state atom lying within the Rydberg wave function have been studied theoretically [32,33] but are challenging to observe in an experiment due to the low probability of finding the right configuration of three atoms. This restriction is of course lifted for bonds to nonexistent ghost atoms [Fig. 2(c)]. The coefficients $c_{nl,x}^b$ for these other Rydberg chemical bonds are provided in the Supplemental Material [20], and it should be remembered that the proposed method is generic to *any* set of coefficients since the key requirement is that only the degenerate n manifold is included. This means that any electronic wave function which is a superposition of nondegenerate states from several n manifolds, e.g., a wave packet or a giant dipole state [34], cannot be created with this scheme. The Stark state [Fig. 2(d)] and the Zeeman state [Fig. 1(b)] highlight that even localized electron wave functions in static fields are entirely different from Rydberg molecule wave functions.

The preparation of these exotic chemical bonds hinges on the fact that Rydberg electrons are strongly affected by external fields. These can manipulate the wave function into classical wave packets [35] or long-lived circular states [36,37]. The enormous extent of Rydberg wave functions creates large transition dipole matrix elements, facilitating easy control even with weak field strengths. The Stark and quadratic Zeeman matrix elements scale as Fn^2 and B^2n^4 , respectively, where F and B are electric and magnetic field amplitudes [18].

The goal of our control scheme is to engineer a final state \vec{c}_f which matches the target state \vec{c}_T . Their similarity is characterized by the fidelity $\Phi = |\langle \vec{c}_T | \vec{c}_f \rangle|^2$. After choosing the field amplitudes and initial ramp times, the final state is determined by the $2N$ time periods: Δt_i^f , when both fields are on, and Δt_i^b , when only the magnetic field is on. Although square pulses are used for simplicity in the present calculations, the error of a finite ramp time in an experiment should still be within the tolerance of our ideal parameter scheme, and a more thorough calculation could certainly include arbitrary pulse shapes to better match experimental conditions. A gradient ascent algorithm finds optimal $\Delta t_i^{b,f}$ parameters giving local maxima in Φ remarkably efficiently. Numerical experiments reveal several generic features of this approach. First, every optimal pulse sequence is primarily determined by the distribution of initial values, typically drawn from a uniform distribution of experimentally realistic values. This implies that there are effectively infinitely many good pulse

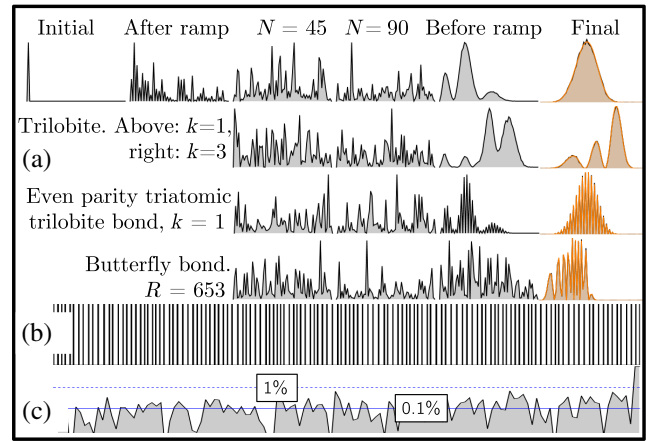


FIG. 3. Details of the proposed scheme for the four orbitals shown in Fig. 2. (a) l distributions, spanning from $l = 0$ on the left to $l = 69$ on the right, at six different times. The first two times, the initial state and the Zeeman state following the field ramp are identical in all cases. The orange overlay in the final state shows the exact target distribution. (b) The field pulses responsible for this $b = 3$ trilobite. The electric fields are turned on in black regions and off in white regions. (c) The fidelity, on a logarithmic scale, as a function of time.

configurations. One of these is shown in Fig. 3(b), and a full data table of this sequence along with others which create the other chemical bonds in Fig. 2 is given in the Supplemental Material [20]. The nonuniqueness of the solutions implies that Φ is not convex, so there is no guarantee that a gradient ascent algorithm will discover global maxima. Surprisingly, our simulations found that, provided enough pulses (typically $N \approx 2n$) of adequate duration (~ 10 's of ns) are used, almost all sequences gave $\Phi > 0.999$. Finally, methods that attempt to increase the fidelity monotonically with each pulse appear impossible. Figure 3(c) shows $\log_{10} \Phi$: at no time prior to the final step of evolution does the fidelity increase above 0.01, nor is it monotonically increasing.

These findings are corroborated by optimal control theory [38]. Quite general quantum proofs exist demonstrating that the topology of quantum control landscapes are very favorable to simple extrema search algorithms [39,40]. Only globally maximal seams exist in a sufficiently large parameter space; local maxima do not exist [41–43]. It is justifiable to restrict the initial guess to realistic experimental values for the field strengths and durations, rather than directly implementing these constraints into the search algorithm. This works excellently given the incredible flexibility of possible solutions [39,44]. The lack of local maxima guarantees that optimal solutions are found rapidly without more complicated genetic algorithms or stochastic optimizers [41].

The complex quantum pathways the wave function evolves along necessitate very stringent control over the field amplitudes and pulse timing. The experiment must be very well shielded from stray fields so that the control field

amplitudes can be specified to better than $10 \mu\text{V}/\text{cm}$ and 1 mG . Rydberg atoms themselves can be used as highly sensitive field sensors [45,46]. The pulse timing should be controlled to femtosecond precision. These error bounds correspond to a 10% reduction in the fidelity from the theoretical prediction. This sensitivity appears to be intrinsic to high Rydberg states, rather than caused by a poorly informed optimal control theory approach. These high sensitivities may require more precise theoretical methods to compute the time evolution as effects beyond first-order perturbation theory are near to this level of accuracy; the proof of principle demonstrated here is still applicable in more sophisticated approaches. A straightforward improvement could include a robustness measure as a cost function in the optimization and use more sophisticated optimization techniques. Recently, this approach successfully obtained optimal radio frequency pulses to excite circular Rydberg states [47], and could similarly ease the experimental difficulties here.

Two experimental methods could directly detect the ghost orbital: electron momentum ($e, 2e$) spectroscopy and x -ray diffraction [20]. In $(e, 2e)$ spectroscopy an energetic electron scatters from and ejects the Rydberg electron; both are detected in coincidence [48,49]. If the electron-electron collision is fully elastic—requiring large momenta, energies exceeding the ionization potential, and large momentum transfer between the electrons—the triply differential cross section is proportional to the electron’s momentum density [48]. Typically only spherically averaged cross sections can be measured in isotropic samples, but since these trilobitelike orbitals are aligned in the

direction of the control fields, the fully differential cross section can be measured.

A complementary technique is x -ray diffraction [50]. The differential scattering cross section for this process is proportional to the Fourier transform of the electron density itself, creating another window into the electronic structure of these ghost orbitals. Figures 4 and 5 show these two different quantities—the momentum density and the Fourier-transformed position density, respectively—for several example ghost orbitals. As expected from Fourier analysis, the momentum-space wave functions in Fig. 4 mirror the symmetries and nodal structure present in the real-space wave functions. Three ridges mirror the nodes in the $b = 3$ trilobite, and the even-parity trimer possesses additional nodes overlapping these ridges showing the absence of odd-parity components. The symmetries in θ_k and k relate to the symmetry of the real-space wave function. The Fourier-transformed electron density has many of these same features, although it is no longer symmetric about $k = 1/n$. It is also significantly smaller in magnitude and less clear to interpret, although the major nodal features corresponding to the trilobite lobes are still apparent [20].

This Letter discussed how exotic ultralong-range ghost chemical bonds consisting of just one atom could be formed and detected in the laboratory. The electron can be forced either to localize very tightly on one or more positions in space, as in the “trilobite,” or to spread out into an exotic fanlike structure, as in the “butterfly.” The control

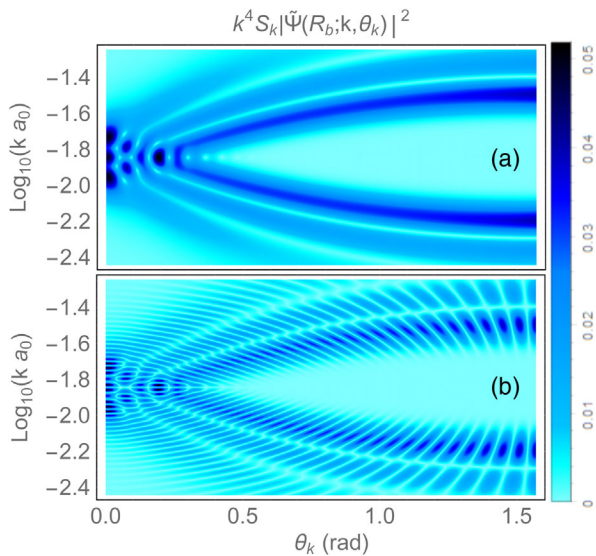


FIG. 4. Momentum-space probability distributions for the $n = 70$, $b = 3$ trilobite dimer (a) and trimer (b). Both are symmetric about $\theta_k = (\pi/2)$ and, when multiplied by k^4 , are logarithmically symmetric about $k = 1/n$. The scaling factor $S_k = (\theta_k + 0.1)$ enhances the visibility at large θ_k .

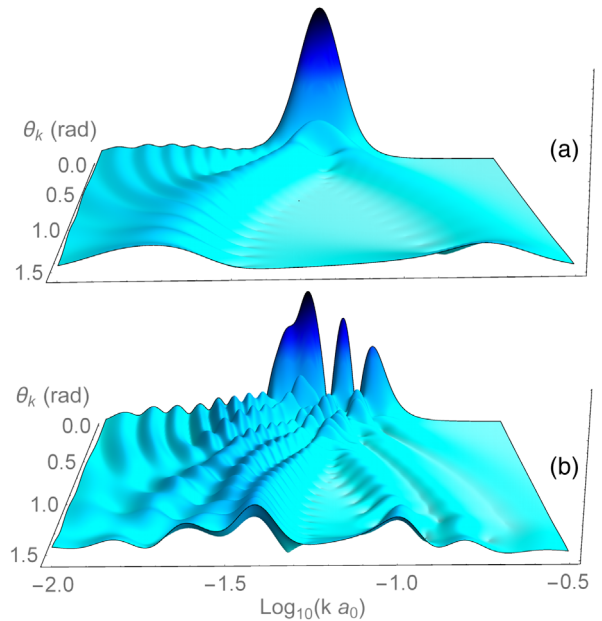


FIG. 5. The quantity $|k^2 F_T(R_b; \vec{k})|$ for the $n = 30$, $b = 1$ and $b = 3$ trilobites. The scaling factor k^2 is added to improve visibility of small features. This function is also symmetric about $\theta_k = (\pi/2)$. $n = 30$ was chosen to connect back to the very first trilobite molecule prediction [5].

scheme, consisting of a slowly varying magnetic field along with a sequence of rapidly pulsed electric fields, emulates the Fermi pseudopotential responsible for the formation of Rydberg molecules by neutral perturbers. The specifics of the field timings are designed efficiently using a gradient ascent algorithm, and excellent fidelity ($\gg 99.9\%$) can be reached with typical laboratory fields and timescales. The stringent control constraints on the field amplitudes and pulse timings, requiring excellent shielding towards stray fields and knowledge of field strengths to high accuracy, are certainly major experimental hurdles reflecting the exaggerated energy scales and complexity of this system, a novel regime for optimal control theory. One can envision even more exotic ghost states for future study, such as extended configurations like the trimer molecules shown here with several more “ghost” atoms spaced along a line [20], or even noncylindrical polyatomic orbitals (requiring $m_l \neq 0$ contributions also). “Electron lattices” could even be envisioned where wave function peaks are placed regularly around the atomic core, with potential applications in quantum gate technology. The theory could be likewise extended to atoms with quantum defects or performed more accurately to include nonperturbative field effects. The proposed detection methods are equally applicable to real Rydberg molecules [51,52].

We are pleased to acknowledge enlightening discussions with F. Robicheaux, R. T. Sutherland, and F. Jafarpour. This work was supported in part by NSF Grant No. PHY-1607180.

-
- [1] V. Bendkowsky, B. Butscher, J. Nipper, J. B. Balewski, J. P. Shaffer, R. Löw, and T. Pfau, Observation of ultralong-range Rydberg molecules, *Nature (London)* **458**, 1005 (2009).
- [2] D. Booth, S. T. Rittenhouse, J. Yang, H. R. Sadeghpour, and J. P. Shaffer, Production of trilobite Rydberg molecule dimers with kilo-Debye permanent electric dipole moments, *Science* **348**, 99 (2015).
- [3] T. Niederprüm, O. Thomas, T. Eichert, C. Lippe, J. Pérez-Ríos, C. H. Greene, and H. Ott, Observation of pendular butterfly Rydberg molecules, *Nat. Commun.* **7**, 12820 (2016).
- [4] E. Fermi, Sopra lo spostamento per pressione delle righe elevate delle serie spettrali, *Il Nuovo Cimento* **11**, 157 (1934).
- [5] C. H. Greene, A. S. Dickinson, and H. R. Sadeghpour, Creation of Polar and Nonpolar Ultra-Long-Range Rydberg Molecules, *Phys. Rev. Lett.* **85**, 2458 (2000).
- [6] J. Tallant, S. T. Rittenhouse, D. Booth, H. R. Sadeghpour, and J. P. Shaffer, Observation of Blueshifted Ultralong-Range Cs₂ Rydberg Molecules, *Phys. Rev. Lett.* **109**, 173202 (2012).
- [7] B. J. DeSalvo, J. A. Aman, F. B. Dunning, T. C. Killian, H. R. Sadeghpour, S. Yoshida, and J. Burgdörfer, Ultralong-range Rydberg molecules in a divalent atomic system, *Phys. Rev. A* **92**, 031403(R) (2015).
- [8] E. L. Hamilton, C. H. Greene, and H. R. Sadeghpour, Shape-resonance-induced long-range molecular Rydberg states, *J. Phys. B* **35**, L199 (2002).
- [9] M. I. Chibisov, A. A. Khuskivadze, and I. I. Fabrikant, Energies and dipole moments of long-range molecular Rydberg states, *J. Phys. B* **35**, L193 (2002).
- [10] K. S. Kleinbach, F. Meinert, F. Engel, W. J. Kwon, R. Löw, T. Pfau, and G. Raithel, Photoassociation of Trilobite Rydberg Molecules via Resonant Spin-Orbit Coupling, *Phys. Rev. Lett.* **118**, 223001 (2017).
- [11] J. Pérez-Ríos, M. T. Eiles, and C. H. Greene, Mapping trilobite state signatures in atomic hydrogen, *J. Phys. B* **49**, 14LT01 (2016).
- [12] M. Tarana and R. Čurík, Adiabatic potential-energy curves of long-range Rydberg molecules: Two-electron *R*-matrix approach, *Phys. Rev. A* **93**, 012515 (2016).
- [13] M. Chibisov, A. M. Ermolaev, F. Brouillard, and M. H. Cherkani, New Summation Rules for Coulomb Wave Functions, *Phys. Rev. Lett.* **84**, 451 (2000).
- [14] B. E. Granger, E. L. Hamilton, and C. H. Greene, Quantum and semiclassical analysis of long-range Rydberg molecules, *Phys. Rev. A* **64**, 042508 (2001).
- [15] J. W. Farley and W. H. Wing, Accurate calculation of dynamic Stark shifts and depopulation rates of Rydberg energy levels induced by blackbody radiation. Hydrogen, helium, and alkali-metal atoms, *Phys. Rev. A* **23**, 2397 (1981).
- [16] T. F. Gallagher and W. E. Cooke, Interactions of Blackbody Radiation with Atoms, *Phys. Rev. Lett.* **42**, 835 (1979).
- [17] F. Zhou and L. Spruch, Temperature-induced transition rates for some hydrogenic states, *Phys. Rev. A* **49**, 718 (1994).
- [18] T. F. Gallagher, *Rydberg Atoms* (Cambridge University Press, Cambridge, England, 2005).
- [19] I. I. Beterov, I. I. Ryabtsev, D. B. Tretyakov, and V. M. Entin, Quasiclassical calculations of blackbody-radiation-induced depopulation rates and effective lifetimes of Rydberg *ns*, *np*, and *nd* alkali-metal atoms with $n \leq 80$, *Phys. Rev. A* **79**, 052504 (2009).
- [20] See Supplemental Material at <http://link.aps.org/supplemental/10.1103/PhysRevLett.121.113203> for calculation details, data tables, additional figures showing position and momentum space densities, and a more detailed discussion of detection schemes, along with Refs. [21–31].
- [21] S.-H. Dong, C.-Y. Chen, and M. Lozada-Cassou, Some recurrence relations among the radial matrix elements for the relativistic hydrogenic atoms, *Phys. Lett. A* **333**, 193 (2004).
- [22] N. Khaneja, T. Reiss, C. Kehlet, T. Schulte-Herbruggen, and S. J. Glaser, Optimal control of coupled spin dynamics: Design of NMR pulse sequences by gradient ascent algorithms, *J. Magn. Reson.* **172**, 296 (2005).
- [23] P. Makotyn, Experimental studies of a degenerate unitary Bose gas, Ph.D. thesis, University of Colorado, 2014.
- [24] A. A. Khuskivadze, M. I. Chibisov, and I. I. Fabrikant, Adiabatic energy levels and electric dipole moments of Rydberg states of Rb₂ and Cs₂ dimers, *Phys. Rev. A* **66**, 042709 (2002).
- [25] B. Podolsky and L. Pauling, The momentum distribution in hydrogen-like atoms, *Phys. Rev.* **34**, 109 (1929).

- [26] S. Cohen, M. M. Harb, A. Ollagnier, F. Robicheaux, M. J. J. Vrakking, T. Barillot, F. Lépine, and C. Bordas, Photoionization microscopy of the lithium atom: Wave-function imaging of quasibound and continuum Stark states, *Phys. Rev. A* **94**, 013414 (2016).
- [27] L. B. Zhao, I. I. Fabrikant, M. L. Du, and C. Bordas, Test of the Stark-effect theory using photoionization microscopy, *Phys. Rev. A* **86**, 053413 (2012).
- [28] P. Giannakeas, F. Robicheaux, and C. H. Greene, Photoionization microscopy in terms of local-frame-transformation theory, *Phys. Rev. A* **91**, 043424 (2015).
- [29] F. Robicheaux, Pulsed field ionization of Rydberg atoms, *Phys. Rev. A* **56**, R3358 (1997).
- [30] R. R. Jones, Creating and Probing Electronic Wave Packets Using Half-Cycle Pulses, *Phys. Rev. Lett.* **76**, 3927 (1996).
- [31] M. J. Cooper, Compton scattering and electron momentum determination, *Rep. Prog. Phys.* **48**, 415 (1985).
- [32] I. C. H. Liu and J. M. Rost, Polyatomic molecules formed with a Rydberg atom in an ultracold environment, *Eur. Phys. J. D* **40**, 65 (2006).
- [33] M. T. Eiles, J. Pérez-Ríos, F. Robicheaux, and C. H. Greene, Ultracold molecular Rydberg physics in a high density environment, *J. Phys. B* **49**, 114005 (2016).
- [34] V. Averbukh, N. Moiseyev, P. Schmelcher, and L. S. Cederbaum, Transition from Rydberg to giant-dipole-moment states of hydrogen atoms in crossed fields: A suggestion for an experiment, *Phys. Rev. A* **59**, 3695 (1999).
- [35] J. Parker and C. R. Stroud, Jr., Coherence and Decay of Rydberg Wave Packets, *Phys. Rev. Lett.* **56**, 716 (1986).
- [36] R. G. Hulet and D. Kleppner, Rydberg Atoms in Circular States, *Phys. Rev. Lett.* **51**, 1430 (1983).
- [37] A. Signoles, E. K. Dietsche, A. Facon, D. Grosso, S. Haroche, J. M. Raimond, M. Brune, and S. Gleyzes, Coherent Transfer between Low-Angular-Momentum and Circular Rydberg States, *Phys. Rev. Lett.* **118**, 253603 (2017).
- [38] C. Brif, R. Chakrabarti, and H. Rabitz, Control of quantum phenomena: Past, present, and future, *New J. Phys.* **12**, 075008 (2010).
- [39] M. Demiralp and H. Rabitz, Optimally controlled quantum molecular dynamics: A perturbation formulation and the existence of multiple solutions, *Phys. Rev. A* **47**, 809 (1993).
- [40] H. A. Rabitz, M. M. Hsieh, and C. M. Rosenthal, Quantum optimally controlled transition landscapes, *Science* **303**, 1998 (2004).
- [41] R. Chakrabarti and H. Rabitz, Quantum control landscapes, *Int. Rev. Phys. Chem.* **26**, 671 (2007).
- [42] B. Russell, H. Rabitz, and R.-B. Wu, Control landscapes are almost always trap free: A geometric assessment, *J. Phys. A* **50**, 205302 (2017).
- [43] K. W. Moore and H. Rabitz, Exploring quantum control landscapes: Topology, features, and optimization scaling, *Phys. Rev. A* **84**, 012109 (2011).
- [44] J. M. Geremia, Wusheng Zhu, and Herschel Rabitz, Incorporating physical implementation concerns into closed loop quantum control experiments, *J. Chem. Phys.* **113**, 10841 (2000).
- [45] A. Facon, E.-K. Dietsche, D. Grosso, S. Haroche, J.-M. Raimond, M. Brune, and S. Gleyzes, A sensitive electrometer based on a Rydberg atom in a Schrödinger-cat state, *Nature (London)* **535**, 262 (2016).
- [46] L. Ma, D. A. Anderson, and G. Raithel, Paschen-Back effects and Rydberg-state diamagnetism in vapor-cell electromagnetically induced transparency, *Phys. Rev. A* **95**, 061804 (2017).
- [47] S. Patsch, D. M. Reich, J.-M. Raimond, M. Brune, S. Gleyzes, and C. P. Koch, Fast and accurate circularization of a Rydberg atom, *Phys. Rev. A* **97**, 053418 (2018).
- [48] C. E. Brion, G. Cooper, Y. Zheng, I. V. Litvinyuk, and I. E. McCarthy, Imaging of orbital electron densities by electron momentum spectroscopy—A chemical interpretation of the binary ($e, 2e$) reaction, *Chem. Phys.* **270**, 13 (2001).
- [49] M. A. Coplan, J. H. Moore, and J. P. Doering ($e, 2e$) spectroscopy, *Rev. Mod. Phys.* **66**, 985 (1994).
- [50] R. W. James, *The Optical Principles of the Diffraction of X-Rays* (Ox Bow, Woodbridge, CT, 1982).
- [51] H.-C. Shao and A. F. Starace, Imaging coherent electronic motion in atoms by ultrafast electron diffraction, *Phys. Rev. A* **88**, 062711 (2013).
- [52] G. Dixit, O. Vendrell, and R. Santra, Imaging electronic quantum motion with light, *Proc. Natl. Acad. Sci. U.S.A.* **109**, 11636 (2012).